International Journal of Nanomedicine

Dovepress
Taylor & Francis Group

Open Access Full Text Article

ORIGINAL RESEARCH

Strike Mitochondria By Enzyme-Instructed Self-Assembled Peptides for Effective Immunogenic Anti-Tumor Therapy

Jingyuan Zhao[1,*], Siyu Tian[1,*], Pengfei Li[2], Huanhuan Wu[2], Shuai Li[1,3], Hong Yuan[1]

[1]Clinical Laboratory Center, Central Hospital of Dalian University of Technology, Dalian, People's Republic of China; [2]College of Laboratory Medicine, Dalian Medical University, Dalian, People's Republic of China; [3]Department of Pharmacy, The First Affiliated Hospital of Dalian Medical University, Dalian, People's Republic of China

*These authors contributed equally to this work

Correspondence: Shuai Li, Department of Pharmacy, The First Affiliated Hospital of Dalian Medical University, Dalian, People's Republic of China, Email shuaili2015@outlook.com; Hong Yuan, Clinical Laboratory Center, Central Hospital of Dalian University of Technology, Dalian, People's Republic of China, Email yuanhonglab@163.com

Introduction: Immunogenic cell death (ICD) plays a crucial role in cancer immunotherapy in disrupting the immunosuppressive tumor microenvironment (TME). However, key bottlenecks remain, including the lack of precise and efficient ICD induction at the tumor site and poor synergy with other therapeutic mechanisms for tumor suppression.

Methods: To tackle these bottlenecks, this study developed a legumain-instructed self-assembling peptide PSK, with legumain highly expressed in tumors. Its mechanism is as follows: first, via sequence design, it specifically binds to programmed cell death ligand 1 (PD-L1), which highly expressed on tumor cells, mediating its selective uptake by tumor cells. Subsequently, catalyzed cleavage by legumain in the TME triggers its in-situ self-assembly into nanoaggregates, prolonging its retention at the tumor site. Finally, the PSK targets the mitochondria of tumor cells, enabling precise organelle-level action.

Results: In vitro and in vivo experiments showed that PSK exerts synergistic anti-tumor effects through a dual mechanism: it targets mitochondria to disrupt membrane potential and induce dysfunction, thereby triggering tumor cell ICD and releasing damage-associated molecular patterns (DAMPs) to activate immunity; meanwhile, it binds to PD-L1 to downregulate its expression, reducing tumor immune escape. As an enzyme-responsive in-situ self-assembling peptide drug, PSK exhibits high tumor cell selectivity, effectively inhibits tumor growth, and has no obvious systemic toxicity.

Discussion: The development of PSK provides a new approach for anti-tumor peptide drug research and precision tumor therapy. With its design featuring tumor specificity, enzyme responsiveness, and dual-action mechanism, this peptide is expected to address key challenges in ICD-based cancer immunotherapy.

Keywords: immunogenic cell death, in-situ assembling, mitochondrial, peptide

Introduction

In recent years, numerous innovative cancer therapies have emerged, with targeted therapy and immunotherapy becoming prominent treatment strategies.[1–3] Despite significant advancements in cancer treatment, the outcomes and prognosis remain unsatisfactory, highlighting the urgent need for more effective therapeutic approaches. Immune checkpoint blockade therapies, such as programmed cell death ligand 1 (PD-L1) inhibitors, have been employed in clinical settings,[4,5] however, their efficacy remains limited due to insufficient immune activation.[6] One promising approach to overcome this limitation is the induction of immunogenic cell death (ICD), which enhances antitumor immune responses by promoting the release of damage-associated molecular patterns (DAMPs) from tumor cells.[7] This process can effectively convert immunologically "cold" tumors into "hot" ones, which are more responsive to immunotherapy.[7] We propose a dual strategy combining ICD induction and PD-L1 pathway blockade to enhance antitumor immunity. However, single-agent ICD inducers often fail to

Received: 2 June 2025
Accepted: 29 October 2025
Published: 6 November 2025

induce robust and durable immune activation due to the complexity of ICD induction and immunosuppressive tumor microenvironment (TME).[7] Consequently, combining ICD inducers with immune checkpoint inhibitors (ICIs) is a rational strategy to achieve synergy,[4] although the efficacy varies and mechanisms are not fully elucidated.[8]

Mitochondria, key regulators of cellular homeostasis, are attractive therapeutic targets due to their role in energy production and apoptosis.[9] Studies indicate that mitochondrial damage-induced oxidative stress can effectively trigger ICD,[10–12] providing a rationale for developing mitochondria-targeted antitumor strategies. Mitochondria in tumor cells often exhibit abnormalities in morphology, quantity, and function,[13,14] features that are closely associated with their proliferative, survival, and metastatic potential,[15] positioning mitochondria as ideal therapeutic targets.

The mitochondria-targeting peptide KLA (KLAKLAKKLAKLAK) is an amphipathic α-helical pro-apoptotic peptide capable of disrupting mitochondrial membrane integrity and inducing apoptosis via the mitochondrial pathway.[16] However, its clinical use is limited by poor cellular uptake, lack of tumor specificity, and potential off-target toxicity.[17] To improve delivery, studies have attempted co-administration with cationic antitumor peptides such as HPRP-A1 to achieve synergistic effects, yet this approach faces uncertainties regarding drug interactions, heterogeneous tissue distribution, and protein binding.[17,18] Alternatively, Li et al employed a matrix metalloproteinase-2 (MMP-2)-responsive cell-penetrating motif to control its toxicity. However, variable MMP-2 activity in normal tissues may lead to off-target effects.[19] Other studies have fused KLA with tumor-specific targeting peptides, which partially improved selectivity, but the monotherapeutic mechanism remains insufficient for achieving durable antitumor efficacy.[20–23]

In situ self-assembly technology utilizes disease-site-specific biochemical signals (eg, enzymes, pH, redox gradients) to induce conformational changes and subsequent nanoassembly of therapeutic molecules at the target site,[24–26] enhancing drug accumulation and retention within tumor tissue. Combining this strategy with enzyme-responsive activation is considered an effective means to enhance the stability and targeting precision of peptide-based drugs.[27–30]

Here, we designed an enzyme-responsive in situ self-assembling peptide, PSK, for targeted and controlled delivery of KLA. PSK comprises four functional modules: a PD-L1 binding peptide,[31] a legumain-responsive cleavage module,[32] a self-assembly domain,[33] and the mitochondrial toxic peptide KLA. The PD-L1 binding peptide specifically targets PD-L1 on tumor cells, facilitating PSK internalization via receptor-mediated endocytosis, thereby enhancing intracellular delivery of KLA. Concurrently, this process promotes PD-L1 internalization and degradation, helping to alleviate immune suppression. Legumain, a protease overexpressed in many tumors but not in normal tissues, specifically cleaves the legumain-responsive linker within lysosomes, triggering the self-assembly module to form β-sheet-rich nanofibers. This assembly disrupts lysosomal membrane integrity, facilitating KLA escape and subsequent mitochondrial targeting, ultimately inducing tumor cell apoptosis. Furthermore, mitochondrial damage can stimulate ICD, enhancing immune cell infiltration and cytotoxic activity within the TME, thereby synergizing with PD-L1 blockade.

By integrating receptor targeting, enzyme-responsive release, and in situ self-assembly, PSK aims to overcome key limitations in KLA delivery and enhance antitumor immunity, providing a novel strategy for co-delivery of ICD inducers and immune checkpoint blockers (ICBs).

Materials and Methods

All multifunctional peptides were acquired from Genscript (China). Human renal cell adenocarcinoma cells (769-P), human embryonic kidney cells (293T), human clear cell renal adenocarcinoma cells (786-O), human colon cancer cells (HCT116), human cervical cancer cells (HeLa 229), and human ovarian cancer cells (SK-OV-3) were obtained from Wuhan Purcelleno (China), while A2780 human ovarian cancer cells were sourced from Shanghai Zeya (China). DMEM medium, RPMI-1640 medium, and 0.25% trypsin-EDTA solution were purchased from Gibco (China), while fetal bovine serum (FBS) was obtained from Wuhan Punosai (China). Legumain purchased from Solarbio (China). Penicillin-streptomycin-gentamicin solution (100×), GreenNuc™ Live Cell Caspase 3 Activity Assay Kit, Mito-Tracker Green, Lyso-Tracker Green, Calcein AM, and PI were sourced from Shanghai Biyuntian Biotechnology Company (China). Cell Counting Kit-8 (CCK8) was acquired from MedChemExpress (USA), Sulfo-Cyanine3 NHS ester was obtained from DuoFluor Inc (China), and Sulfo-Cyanine5 NHS ester was sourced from MACKLIN (China). Primary antibodies included: anti-Hsp70 (Proteintech, #66183-1-Ig), anti-Bax (HuaBio, #ET1603-34), anti-Bcl-2 (Abcam, #T40056F), and anti-GAPDH (Thermo Fisher Scientific, #MA5-15738). Secondary antibodies included: anti-mouse or rabbit horseradish

peroxidase (HRP)-conjugated secondary antibody (Thermo Fisher Scientific, #31400, #31464), and 488-labeled fluorescent mouse or rabbit secondary antibody (Proteintech, #RGAR002, #RGAM002).

Cell Culture Study on Antitumor Activity of Enzyme-Instructed Self-Assembling Peptides

769-P, 786-O, and A2780 cells were cultured in RPMI-1640 medium supplemented with 10% FBS and 1% penicillin-streptomycin-gentamicin solution (100×) at 37°C in a 5% CO2 atmosphere. 293T, HCT116, Hela 226, and SK-OV-3 cells were cultured in DMEM medium containing 10% FBS and 1% penicillin-streptomycin-gentamicin solution (100×) at 37°C with 5% CO2.

Synthesis and Characterization of Self-Assembling Peptides

All peptides used in this experiment were synthesized via solid-phase FMOC (9-fluorenylmethoxycarbonyl) chemistry. The synthesis proceeded from the C-terminus to the N-terminus through sequential coupling of amino acid residues. Upon completion of the full sequence, side-chain protecting groups were removed, and the target peptide was cleaved from the resin to obtain the crude product.

To verify the purity and structural integrity of the synthesized peptides, the following analytical techniques were employed: (1) Reversed-phase high-performance liquid chromatography (RP-HPLC):[17] Peptide samples were separated and detected using RP-HPLC. Chromatograms were recorded to determine retention times and retention indices of various components, allowing evaluation of sample purity and impurity profiles. (2) MS: Purified peptide samples from RP-HPLC were subjected to MS analysis. Acquired mass spectra were interpreted based on molecular ion peaks and characteristic fragment ions to confirm the molecular weight and primary structure of the target peptide. (3) CD spectroscopy:[34] Highly purified peptide samples were dissolved in an appropriate solvent ensuring complete dissolution and absence of visible impurities. The sample was loaded into a quartz cuvette, and spectral scans were performed under optimized parameters (eg, wavelength range, scan rate) tailored to peptide properties. Characteristic CD signals (such as negative peaks at 208 nm for α-helices and 217 nm for β-sheets) were used to analyze secondary structure composition. (4) TEM: A small volume of peptide solution was deposited onto a carbon-film-coated copper grid and allowed to adsorb. The sample was negatively stained, air-dried, and optionally stabilized with a fixative. Images were acquired at appropriate acceleration voltages and magnifications to examine the microstructure and morphology of the peptide assemblies.

For pre-experimental processing, peptide powders were first dissolved in dimethyl sulfoxide (DMSO) to prepare high-concentration stock solutions. These were then diluted stepwise with sterile distilled water to the desired working concentrations. All diluted solutions were clear, homogeneous, and free of precipitate before use.

Cellular Uptake Assay

Peptide (0.5 mg) was dissolved in 1 mL of sodium bicarbonate solution (pH 8.3), followed by the addition of 500 μL of Cy3 or Cy5 dye solution. The mixture was incubated overnight at 4 °C with gentle agitation under light-protected conditions. The reaction solution was then transferred to a 3 kDa molecular weight cutoff (MWCO) ultrafiltration device, diluted with 1 mL of 1× phosphate-buffered saline (PBS), and centrifuged at 3000 rpm for 10 minutes. The retained fraction in the upper chamber was collected for subsequent applications.[35]

769-P cells were seeded into laser confocal petri dishes and cultured overnight to allow complete adhesion. Each dish was treated with 500 μL of diluted fluorescent peptide and incubated under light-protected conditions. At predetermined time points, the compound was removed to terminate uptake, and the cells were washed three times with 1× PBS for 5 minutes each. Subsequently, the cells were stained with Hoechst 33342 nucleic acid stain (diluted 1:1000) for 15 minutes in the dark. Finally, the samples were imaged using a laser scanning confocal microscope (LSCM).[36,37]

Lysosomal Escape and Drug Mitochondrial Co-Localization Experiments

According to the experimental schedule, cells were treated with compounds at specified time points. Subsequently, 1 mL of nuclear staining solution was added per laser confocal petri dish and incubated for 15 minutes protected from light.

Lyso-Tracker Green working solution was diluted 1:1000, pre-warmed to 37 °C, applied to the cells, and incubated for 60 minutes. For mitochondrial staining, Mito-Tracker Green was diluted 1:5000, pre-warmed, and incubated with the cells at 37 °C for 15–45 minutes. Imaging was performed using a LSCM.[20]

Cell Proliferation Assays

Cells in the logarithmic growth phase were seeded into 96-well plates at a density of 10,000 cells per well. Following cell attachment, compounds were administered and the plates were incubated for 24 hours. After treatment, CCK-8 reagent was added to each well and incubated for 1–2 hours. Absorbance at 450 nm was measured using a microplate reader to determine relative cell viability.[38]

Colony Formation Assay

769-P cells in the logarithmic phase were plated into 12-well plates at a density of 1000 cells per well. After adherence, the culture medium was replaced with fresh medium containing the designated drug(s). The cells were cultured for 7–14 days, with the drug-containing medium refreshed every 4 days. Once macroscopic clones had formed, the culture was terminated. The cells were gently washed twice with 1× PBS, fixed with 4% paraformaldehyde for 15–30 minutes, and then rinsed again with PBS. Staining was performed with 0.2% crystal violet for 10 minutes. After recovering the staining solution, the plates were rinsed under slow-running water, air-dried, and imaged for subsequent analysis.[39]

Tumor Cell Spheroid Formation Assay

Following autoclaving, the bottom of each well in a 6-well plate was evenly coated with agar-based medium. 769-P cells in the logarithmic growth phase were harvested and seeded into the plates at a density of 1000 cells per well. An appropriate volume of drug-containing medium was then prepared and added to each well. The plates were gently swirled to ensure even distribution of the medium. Cells were cultured for 7–14 days, after which colony formation was assessed across treatment groups and the control.[38]

Western Blotting

Total protein was extracted by lysing cells in RIPA buffer containing 1% PMSF on ice. The lysates were separated by 12.5% SDS-PAGE and subsequently transferred to PVDF membranes. After blocking with 4% bovine serum albumin in TBST for 0.5 hour with gentle shaking, the membranes were incubated with specific primary antibodies at 4 °C overnight. Following three washes with TBST, the membranes were probed with HRP-conjugated secondary antibodies diluted at 1:2000 for 1 hour at room temperature. Protein bands were visualized using an enhanced chemiluminescence (ECL) detection system.[36]

Cell Death Assay

Cell death was assessed using a Calcein AM/PI cell viability and cytotoxicity assay kit. Briefly, Calcein AM and PI were diluted in the provided buffer, applied to the cells, and incubated at room temperature for 20 minutes protected from light. After washing with PBS, the samples were imaged under an inverted fluorescence microscope.[37]

Mitochondrial Membrane Potential Detection Assay

Mitochondrial membrane potential was evaluated using the JC-1 assay. Cells were incubated with freshly prepared JC-1 working solution for 20 minutes at 37 °C in the dark. Following incubation, the solution was removed, and the cells were gently washed with PBS before immediate examination under an inverted fluorescence microscope.[40]

Transcriptome Sequencing Analysis

Following 24 hours of continuous PSK treatment, total RNA was extracted from 769-P cells using TRIzol reagent. The RNA samples were then submitted to Novogene (China) for subsequent RNA extraction quality control, library preparation, and transcriptome sequencing. Differential gene expression analysis was performed based on the sequencing results. The identified DEGs were further subjected to Gene Ontology (GO) enrichment and KEGG pathway analysis.[41]

Caspase 3 Activity Assay

Cells were treated with the drug for 24 hours under standard culture conditions. After treatment, the cells were washed with 1× PBS and incubated with a fluorescently labeled Caspase 3 antibody for 30 to 60 minutes. Following removal of the staining solution and an additional PBS wash, the nuclei were counterstained. Images were acquired using an inverted fluorescence microscope.[42]

ROS Assay

Following 24 hours of drug treatment, the culture medium was aspirated and the cells were washed with 1× PBS. Then, 400 μL of DCFH-DA working solution (diluted 1:1000 in serum-free medium) was added to each well and incubated for 15–20 minutes protected from light. After gently washing with PBS, 400 μL of nuclear staining solution was applied and incubated for another 15 minutes under light-free conditions. Finally, the cells were visualized and imaged using an inverted fluorescence microscope.[36]

Cellular Immunofluorescence

After 24 hours of drug treatment, 769-P cells were washed with PBS and fixed with pre-cooled methanol for 10–15 minutes. The cells were then blocked with 5% bovine serum albumin at room temperature for 1.5 hours. Subsequently, they were incubated with an anti-CRT primary antibody (diluted 1:1000) overnight at 4 °C. Following three washes with PBS (5 minutes each), the cells were incubated with a fluorescent secondary antibody (diluted 1:500) for 1 hour at room temperature in the dark. After another three PBS washes, nuclei were stained and incubated for 20 minutes protected from light. Images were acquired using an inverted fluorescence microscope.[38]

The in-vivo Studies Using Animal Model

For in vivo fluorescence imaging, tumor-bearing nude mice were intravenously injected with Cy5-labeled PSK and KLA via the tail vein 6 h and 24 h prior to imaging, respectively. The mice were anesthetized and placed in an imaging chamber for signal acquisition. Biodistribution and targeting efficiency were evaluated based on the fluorescence images.

For the xenograft model, the culture medium of 768-O and HCT116 cells was replaced one day before harvesting. When cells reached 80–90% confluence, they were detached, washed twice with ice-cold 1× PBS, and resuspended in serum-free medium. The cell density was adjusted to 10^8 cells/mL and mixed with Matrigel at a 1:2 ratio (cell suspension: Matrigel). A 150 μL aliquot of the mixture was subcutaneously injected into the flank of each nude mouse. The entire procedure was completed within 30 min with the cell suspension maintained on ice. Tumor growth was monitored regularly. Once the tumor volume reached a predetermined size, drugs were administered via tail vein injection every two days. Body weight and tumor size were recorded throughout the study. Tumor volume was calculated as $V = 1/2 \times \text{length} \times \text{width}^2$.

At the experimental endpoint, blood samples were collected from the orbital sinus and allowed to clot at room temperature for 2 h. Serum was separated by centrifugation at 3000 rpm for 10 min and stored at -20 °C for subsequent analysis of cancer-related biomarkers. The mice were euthanized, and tumors along with major organs (heart, liver, spleen, lungs, and kidneys) were harvested for further analysis. Fresh tissues were fixed in 4% paraformaldehyde for 24 h, dehydrated in 30% sucrose solution for at least 48 h, embedded in OCT compound, and sectioned into 5–10 μm slices. Sections were air-dried at room temperature for 30 min and stored at -20 °C for subsequent TUNEL assay and immunofluorescence staining.[36,38]

Statistical Analysis and Graphing

All experiments were carried out with at least three biological replicates, and Image J was used to analyze and count the images. Graph Pad Prism 8 was used for data analysis and graphing. Unpaired *t*-test was used for comparison between two groups, and one-way ANOVA was used for comparison between two or more groups. Differences were considered statistically significant (*$p < 0.05$; **$p < 0.01$; ***$p < 0.001$; ****$p < 0.0001$).

Result

Design, Synthesis and Characterization of PSK

The peptide PSK (KLAKLAKKLAKLAK-KLVFF-AAN-CVRARTR) comprises four functional modules: (1) PBP (CVRARTR), which serves as a PD-L1 blocking peptide and enables cancer cell targeting; (2) AAN, a legumain-specific enzymatic cleavage site; (3) KLVFF, a self-assembling motif driven by hydrophobic interactions; (4) KLA, a mitochondrial-disrupting domain that induces apoptosis. For comparative studies, PSK along with its individual components PBP and KLA were synthesized separately. As illustrated in Figure S1, successful synthesis was confirmed using high-performance liquid chromatography (HPLC) and mass spectrometry (MS), with observed molecular weights of 861.0 Da for PBP, 1524.0 Da for KLA, and 3258.5 Da for PSK.

The enzymatic responsiveness of PSK was evaluated using transmission electron microscopy (TEM). Prior to legumain treatment, PSK in aqueous solution exhibited no distinct aggregates (Figure 1A). However, upon incubation with legumain, PSK self-assembled into well-defined nanofilament structures.

The secondary structural changes of PSK in response to legumain were further investigated by circular dichroism (CD) spectroscopy. Typical CD signatures include a negative peak near 208 nm for α-helices and another around 216–218 nm for β-sheet conformations. As shown in Figure 1B, untreated PSK displayed a negative peak at 200 nm, indicative of α-helical content. Following legumain treatment, this peak disappeared and a new negative peak emerged near 220 nm, confirming a structural transition from α-helix to β-sheet. These results demonstrate that legumain triggers the self-assembly of PSK into β-sheet-rich nanostructures.

Cellular Uptake of PSK

To evaluate the cellular internalization of PSK and KLA in vitro, we conducted fluorescence-based uptake assays. Both peptides were labeled with Cy3, a red-fluorescent dye, and incubated with 769-P cells for 5 hours. As shown in Figure 1C, no red fluorescence was detected in cells treated with KLA, indicating limited cellular uptake. In contrast, strong red fluorescence was observed in the PSK-treated group, demonstrating significantly enhanced cellular internalization of PSK. To verify whether the PD-L1-binding domain of PSK interacts with PD-L1 on the surface of tumor cells and promotes the internalization of PSK via endocytosis, we designed a cellular uptake experiment: the PD-L1-binding peptide CVRARTR was added at the same concentration as PSK, and co-incubated with PSK for 5 hours to evaluate its potential to competitively bind PD-L1 and thereby affect PSK uptake. The results (Figure 1D) showed that the addition of exogenous CVRARTR significantly reduced the internalization efficiency of PSK. This finding indicates that the internalization process of PSK specifically depends on the interaction between its CVRARTR domain and PD-L1 expressed on the surface of tumor cells.

To investigate the subcellular localization of PSK, we used Lyso-Tracker Green—a lysosome-specific fluorescent probe that labels acidic organelles in live cells. 769-P cells were treated with PSK-Cy3 and co-stained with Lyso-Tracker Green and a nuclear stain. As illustrated in Figure 1E, partial co-localization was observed, suggesting that PSK is internalized into lysosomes while also exhibiting evidence of lysosomal escape and subsequent accumulation in the cytosol.

We further examined whether PSK targets mitochondria after cellular entry using Mito-Tracker Green, a membrane potential-independent mitochondrial stain. Cells were incubated with PSK-Cy3 for 5 hours and then stained with Mito-Tracker Green and a nuclear dye. Confocal imaging revealed clear co-localization of PSK-Cy3 with mitochondrial signals (Figure 1F), confirming that PSK efficiently localizes to mitochondria following internalization.

PSK Effectively Kills Cancer Cells

The self-assembling peptide PSK, constructed from the PD-L1-blocking peptide PBP and the mitochondrial toxic peptide KLA linked via enzyme-responsive motifs and assembly domains, was designed to enhance both safety and antitumor efficacy. To evaluate its therapeutic potential, we compared four treatment regimens—PBP, KLA, PBP+KLA, and PSK—on both 769-P cancer cells and non-tumorigenic 293T cells. Cell viability assays revealed that PBP, KLA, and the PBP +KLA combination had minimal cytotoxic effects on either cell line (Figure 2A and B). In contrast, PSK induced significant cell death in 769-P cells in a dose-dependent manner, with notable efficacy even at a low concentration (12.5 μM). Importantly, at the same concentration, PSK did not impair the viability of 293T cells, indicating a favorable

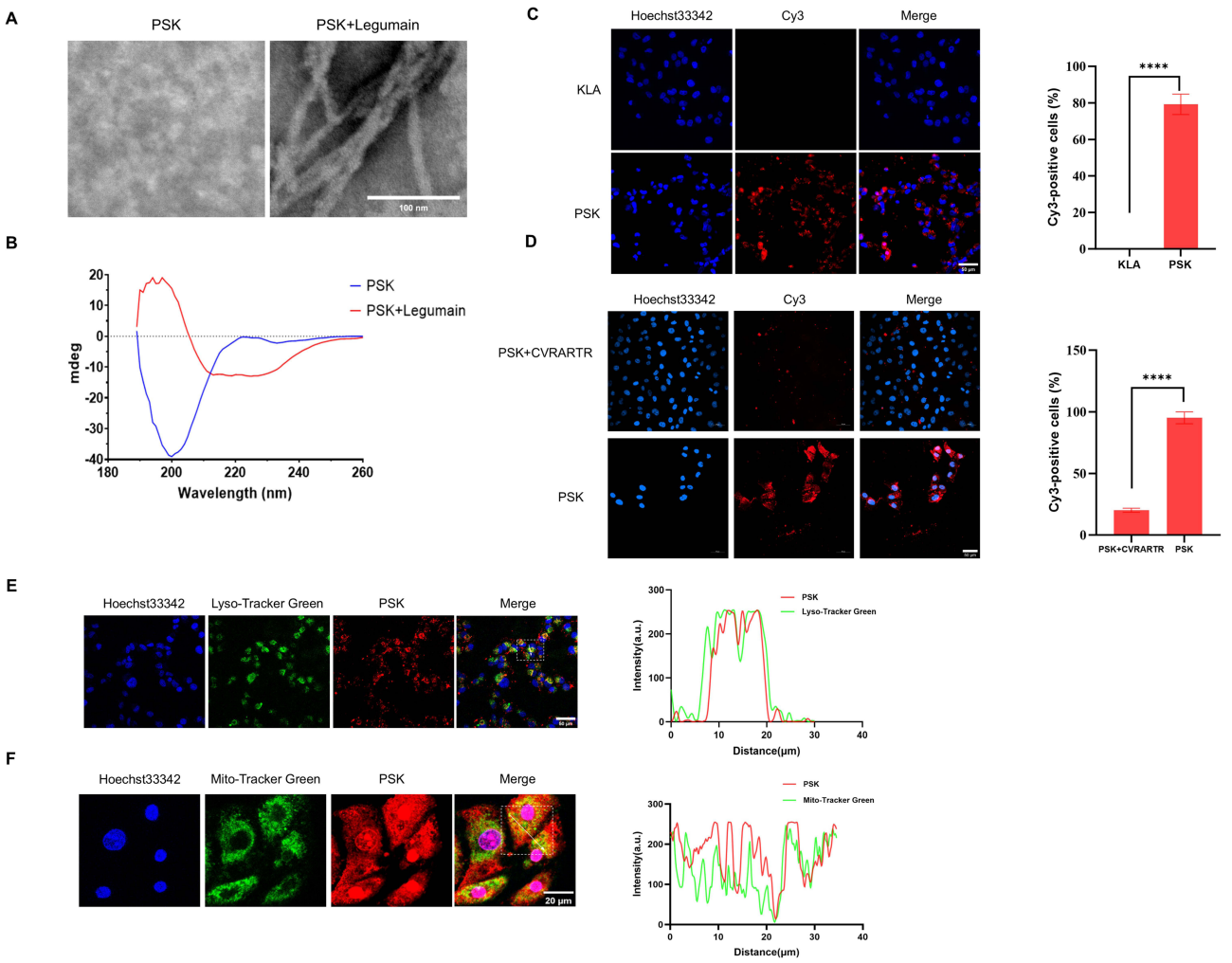

Figure 1 Enzyme-responsive self-assembly and cellular uptake of PSK. (**A**) TEM images of PSK: (left) monomeric form of PSK; (right) morphology of PSK after incubation in legumain-containing solution (scale bar: 100 nm). (**B**) Secondary structure analysis of PSK by CD spectroscopy. (**C**) Fluorescence images and quantitative analysis of 769-P cells incubated with Cy3-labeled KLA (red) or PSK for 5 h. Nuclei were stained with Hoechst 33342 (blue) (scale bar: 50 μm). (**D**) Fluorescence images and quantitative analysis of 769-P cells incubated with Cy3-labeled PSK (red) and PD-L1-binding peptide CVRARTR for 24 h. Nuclei were stained with Hoechst 33342 (blue) (scale bar: 50 μm). (**E** and **F**) Fluorescence images and co-localization analysis of 769-P cells pre-treated with lysosomal (green) or mitochondrial (green) probes followed by incubation with Cy3-labeled PSK (red) for 5 h. Nuclei were stained with Hoechst 33342 (blue) (scale bar: 50 μm). (****p < 0.0001).

safety profile (Figure 2C). To further assess the broad-spectrum antitumor activity of PSK, we treated multiple cancer cell types—including renal, ovarian, cervical, and colorectal cancer cells—with PSK. The results demonstrated potent antitumor effects across these diverse malignancies (Figure 2D).

Western blot analysis revealed substantially higher PD-L1 expression in 769-P cells compared to 293T cells (Figure 2E), suggesting that PD-L1 may facilitate PSK internalization via endocytosis, thereby enhancing its antitumor potency. We also examined PD-L1 expression in 769-P cells following treatment with KLA or PSK. While KLA treatment did not alter PD-L1 levels, PSK significantly downregulated PD-L1 expression (Figure 2F).

To elucidate the mechanism of PSK action, we investigated its dependence on PD-L1-mediated endocytosis and subsequent lysosomal enzyme activation. A competitive binding assay showed that increasing concentrations of PBP inhibited the cytotoxic effect of PSK (Figure 2G), consistent with competition for PD-L1 binding sites. This supports the hypothesis that PSK enters cells via PD-L1-mediated endocytosis. Furthermore, since PSK requires legumain-mediated cleavage in the lysosome for activation, we evaluated its activity in the presence of chloroquine, a lysosomal inhibitor. As anticipated, chloroquine treatment suppressed PSK-induced cell death in a concentration-dependent manner (Figure 2H), underscoring the essential role of lysosomal legumain in PSK activation.

https://doi.org/10.2147/IJN.S544253

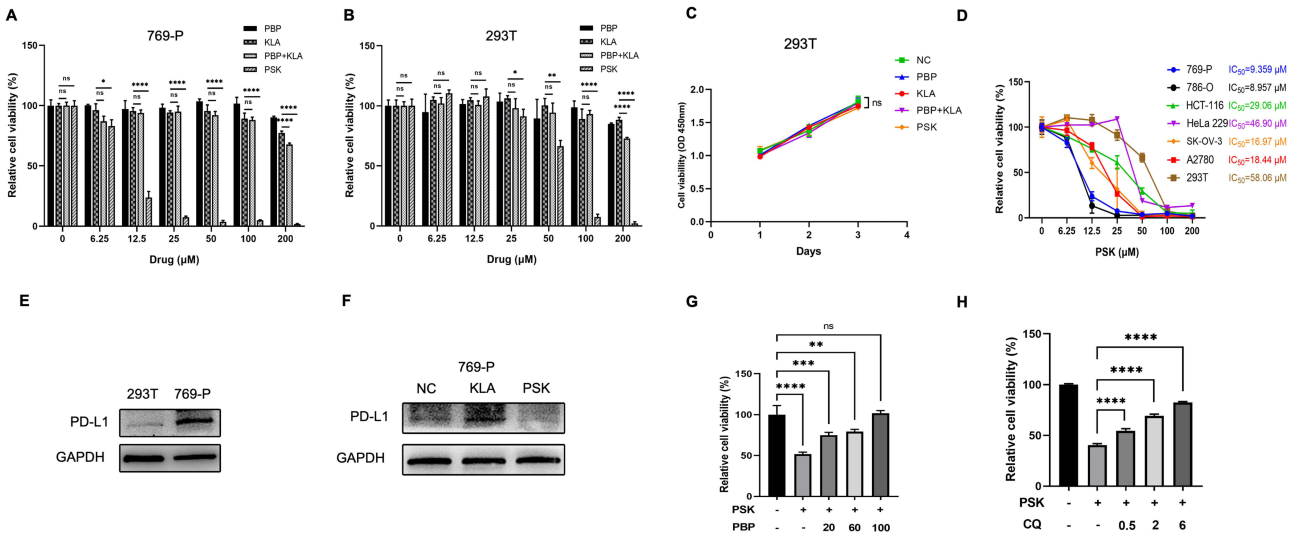

Figure 2 PSK selectively kills tumor cells in vitro through PD-L1-mediated endocytosis. (**A**) Relative viability of 769-P cells treated with different concentrations of PBP, KLA, PBP+KLA, and PSK. (**B**) Relative viability of 293T cells treated with different concentrations of PBP, KLA, PBP+KLA, and PSK. (**C**) Relative viability of 293T cells treated with PBP, KLA, PBP+KLA, and PSK. (**D**) Comparison of PSK sensitivity across multiple cell lines. (**E**) PD-L1 expression levels in 293T and 769-P cells. (**F**) PD-L1 expression after treatment with KLA and PSK. (**G**) Competitive inhibitory effect of PBP on PSK. (**H**) Inhibitory effect of chloroquine on PSK. (NC, negative control; ns, not significant; *p < 0.05; **p < 0.01; ***p < 0.001; ****p < 0.0001).

PSK Induces Tumor Cell Apoptosis and ICD

To further evaluate the impact of PSK on tumor cell proliferation, we performed colony formation assays. The results demonstrated that KLA treatment did not significantly affect the proliferative capacity of 769-P cells compared to the control group (Figure 3A). In contrast, PSK treatment markedly inhibited colony formation, indicating superior inhibitory activity relative

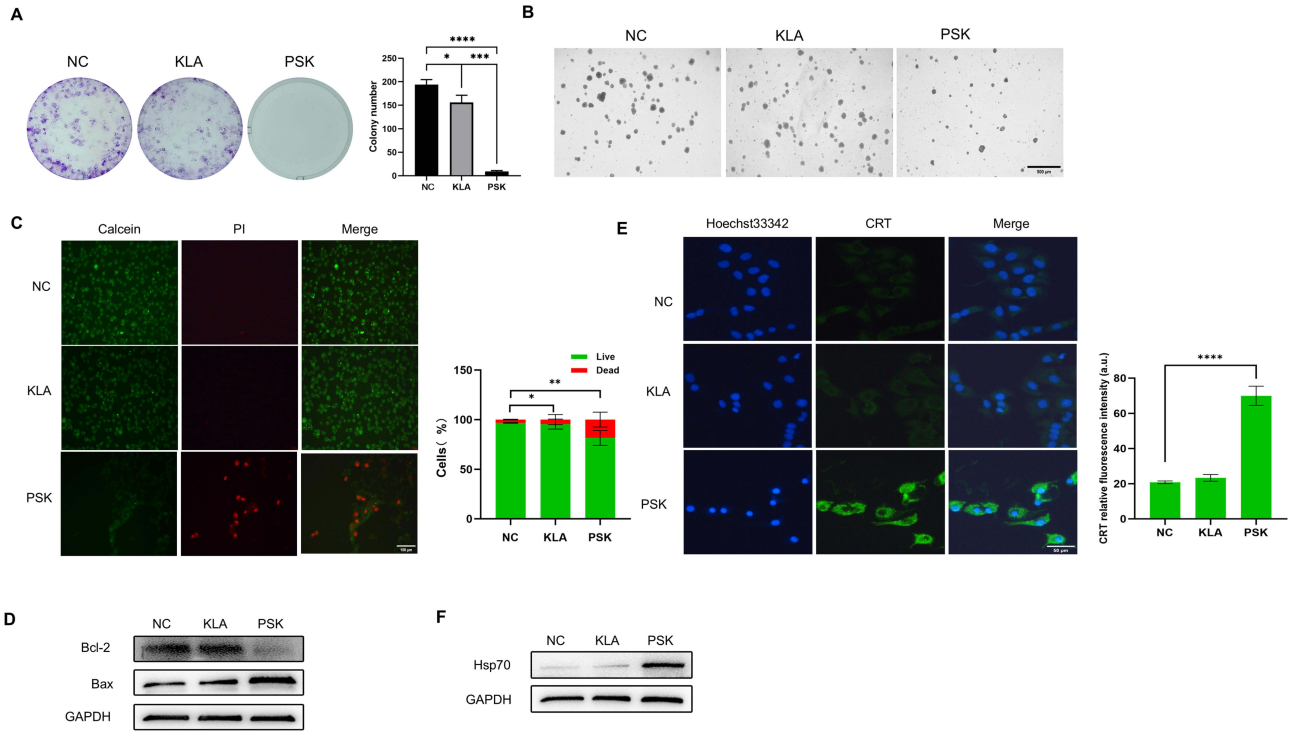

Figure 3 PSK inhibits colony formation and induces immunogenic cell death. (**A**) Colony formation assay of 769-P cells treated with KLA or PSK to evaluate single-cell proliferative capacity. (**B**) Tumor spheroid penetration and killing assay of 769-P cells treated with KLA or PSK (scale bar: 500 μm). (**C**) Fluorescence images and quantitative analysis of Calcein-AM (green, live cells) and PI (red, dead cells) double-stained 769-P cells after treatment with KLA or PSK (scale bar: 100 μm). (**D**) Expression levels of Bax and Bcl-2 in 769-P cells after treatment with KLA or PSK. (**E**) Immunofluorescence images showing CRT (green) translocation in 769-P cells after treatment with KLA or PSK. Nuclei were stained with Hoechst 33342 (blue) (scale bar: 50 μm). (**F**) Expression of Hsp70 in 769-P cells after treatment with KLA or PSK. (NC, negative control; *p < 0.05; **p < 0.01; ***p < 0.001; ****p < 0.0001).

to KLA alone. To better simulate in vivo tumor growth and assess the penetrability and antitumor efficacy of PSK within tissue-like structures, we established tumor spheroid models. PSK treatment resulted in fewer and smaller tumor spheroids compared to both control and KLA-treated groups (Figure 3B), suggesting enhanced penetration and killing capacity. We further compared the cytotoxic effects of PSK and KLA using Calcein-AM and propidium iodide (PI) staining to distinguish viable and dead cells. While no significant difference was observed between KLA and control groups, PSK treatment substantially reduced the number of live cells and increased cell death (Figure 3C), confirming the stronger antitumor activity of PSK at equal concentrations. At the protein level, Western blot analysis revealed that KLA treatment did not alter the expression levels of the apoptosis-related proteins Bax and Bcl-2. In contrast, PSK significantly upregulated Bax and downregulated Bcl-2 (Figure 3D), indicating activation of mitochondrial apoptosis.

ICD is a process wherein dying tumor cells enhance immunogenicity by releasing DAMPs, promoting T-cell infiltration, and converting immunologically "cold" tumors into "hot" tumors.[43] Given that mitochondrial damage can trigger ICD,[44] we investigated whether PSK induces ICD. Immunofluorescence staining for calreticulin (CRT) exposure, a hallmark of ICD, showed weak CRT signal in both control and KLA-treated groups. In contrast, PSK treatment strongly enhanced CRT translocation (Figure 3E), indicating induction of ICD. Consistently, PSK also significantly upregulated the expression of heat shock protein 70 (Hsp70), another ICD marker, while KLA had no such effect (Figure 3F). These results collectively demonstrate that PSK robustly induces ICD in tumor cells.

Research on the Mechanism of PSK Action

To investigate the mechanism underlying PSK-induced apoptosis, we first measured the activity of caspase-3, a key executor of apoptosis. As shown in Figure 4A, PSK treatment resulted in a marked increase in green fluorescence intensity, indicating significantly enhanced caspase-3 activity. This suggests that PSK triggers apoptosis and commits cells to an irreversible death pathway. To determine whether PSK induces cell death through mitochondrial disruption, we assessed mitochondrial membrane potential using the JC-1 fluorescent probe. In healthy cells, JC-1 forms aggregates emitting red fluorescence, whereas in apoptotic cells, depolarized mitochondria lead to JC-1 monomer formation and green fluorescence. After 24 hours of PSK treatment, a pronounced reduction in red fluorescence and a concomitant increase in green fluorescence were observed (Figure 4B), confirming mitochondrial membrane depolarization and the induction of apoptosis. Since oxidative stress is a known activator of apoptotic pathways, we also measured intracellular reactive oxygen species (ROS) levels using the DCFH-DA probe. PSK-treated cells exhibited substantially enhanced green fluorescence compared to controls (Figure 4C), indicating a significant increase in ROS production and implying that PSK induces oxidative damage in cancer cells.

To gain further insight into the mechanism of action of PSK, we performed transcriptome sequencing on 769-P cells following treatment. PSK administration led to the upregulation of 331 genes and downregulation of 537 genes (Figure 4D). Functional enrichment analysis of these differentially expressed genes (DEGs) revealed that GO terms were significantly associated with cell development, differentiation, and immune processes (Figure 4E). Kyoto Encyclopedia of Genes and Genomes (KEGG) pathway analysis indicated that PSK modulates several critical cancer-related signaling pathways, including the general cancer pathway, PI3K-Akt, and MAPK pathways (Figure 4F).

In vivo Antitumor Effects of PSK

To evaluate the biodistribution of PSK and KLA in vivo, Cy5-labeled peptides were administered intravenously to nude mice via the tail vein. Drug distribution was monitored at 6 h and 24 h post-injection. Due to the poor tumor-forming capacity of 769-P cells, which hindered the establishment of a reliable subcutaneous tumor model, we utilized 786-O renal cancer cells—which also exhibit high sensitivity to PSK—for subsequent in vivo imaging studies. As shown in Figure 5A, pronounced tumor accumulation of PSK was observed at the 6 h time point, whereas KLA showed no specific targeting to the tumor site. Ex vivo imaging at 24 h further confirmed sustained accumulation of PSK in tumor tissue, in contrast to KLA, which still exhibited no discernible targeting (Figure 5B). The above experimental results confirmed that PSK exhibited significantly enhanced tumor-targeting ability in vivo. Traditional nanoplatforms mainly rely on passive accumulation through the enhanced permeability and retention (EPR) effect, such as Y8 NPs[38] and CECMa,[36] or strategies such as chemotherapy combined with phototherapy are employed to synergistically enhance antitumor

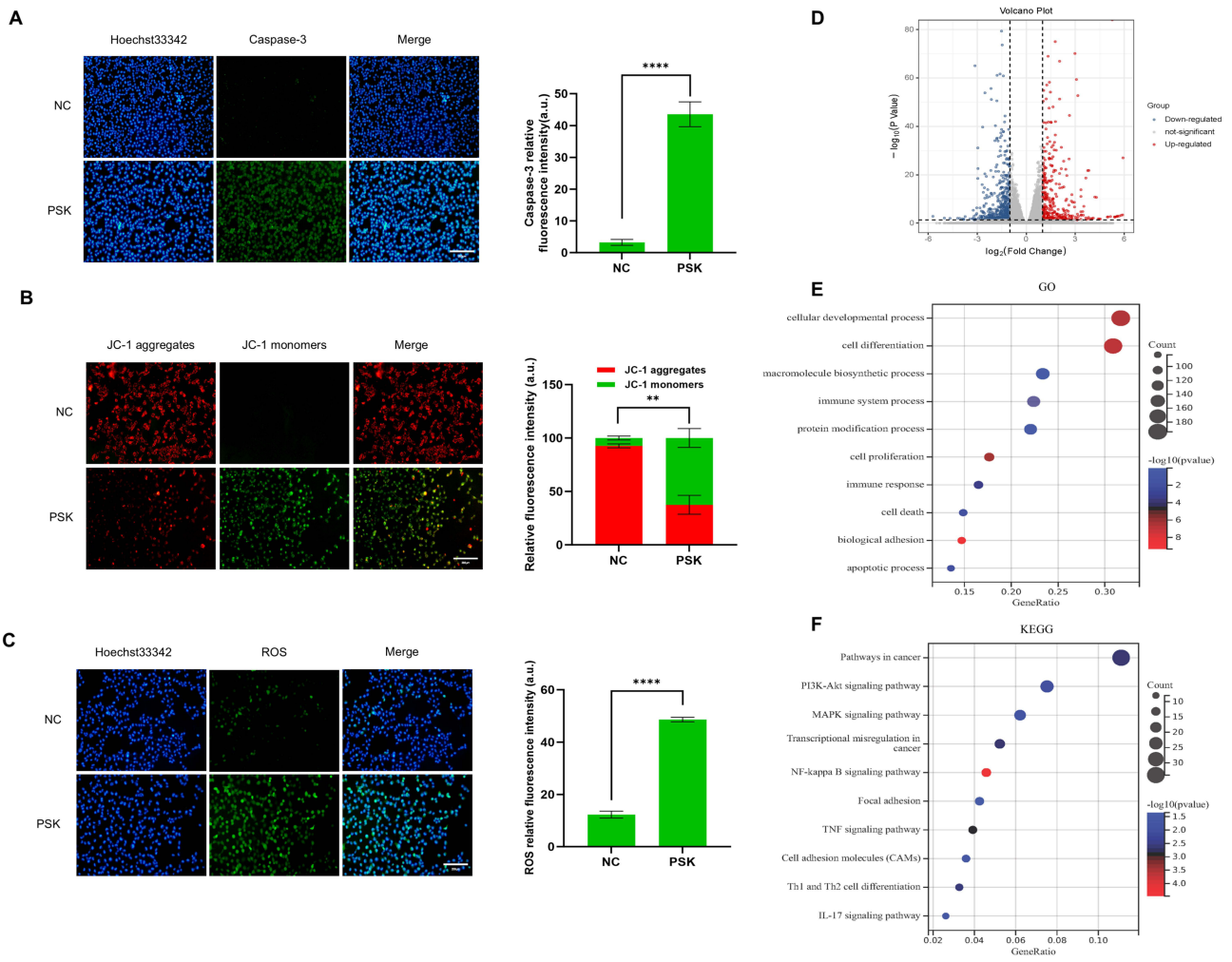

Figure 4 PSK induces mitochondrial damage, ROS generation, and subsequent apoptosis through multiple pathways. (**A**) Fluorescence images and quantitative analysis of 769-P cells treated with PSK and incubated with Caspase 3 antibody working solution (green). Nuclei were stained with Hoechst 33342 (blue) (scale bar: 200 μm). (**B**) Fluorescence images and quantitative analysis of 769-P cells treated with PSK and incubated with JC-1 working solution. In normal cells, JC-1 forms aggregates in the mitochondrial matrix (red fluorescence); during early apoptosis, mitochondrial membrane potential decreases, and JC-1 exists as monomers (green fluorescence) (scale bar: 200 μm). (**C**) Fluorescence images and quantitative analysis of 769-P cells treated with PSK and incubated with DCFH-DA working solution (green). Nuclei were stained with Hoechst 33342 (blue) (scale bar: 200 μm). (**D**) Transcriptomic profiling of 769-P cells after PSK treatment compared to untreated control. The x-axis represents fold change (FC), and the y-axis shows the negative base-10 logarithm of the p-value from *t*-test. Black dashed lines indicate screening thresholds. Red dots represent significantly upregulated genes (n=331), blue dots indicate significantly downregulated genes (n=537), and gray dots show non-DEGs. (**E**) GO biological process enrichment bubble plot and (**F**) KEGG pathway enrichment bubble plot of DEGs. The x-axis represents the ratio of DEGs in each pathway, the y-axis shows GO or KEGG pathway names. Bubble color corresponds to p-value (redder color indicates smaller p-value and higher significance), and bubble size represents the number of differentially enriched genes (larger bubbles indicate more genes). (**p < 0.01; ****p < 0.0001).

Abbreviation: NC, negative control.

immunity, thereby improving the selectivity and therapeutic efficacy of nanodelivery systems. In contrast, PSK adopts an enzyme-responsive in situ self-assembly approach, enabling prolonged retention at tumor sites. Remarkably, clear fluorescence signals could still be observed 24 hours after intravenous injection, in contrast, Y8 NPs[38] showed predominant accumulation in the kidneys and liver, underscoring its excellent targeting capability and sustained localization characteristics.

We next assessed the antitumor efficacy of PSK using subcutaneous xenograft models established with 786-O and HCT 116 cells. Mice were randomly assigned to three groups and received intravenous injections of saline, KLA (2.4 mg/kg), or PSK (5 mg/kg). Tumor growth was not significantly inhibited in the KLA-treated group, whereas PSK treatment resulted in marked suppression of tumor progression compared to the control group (Figure 5C and D). TUNEL staining revealed extensive apoptosis in tumors from the PSK-treated group (Figure 5E and F), consistent with potent tumor cell killing.

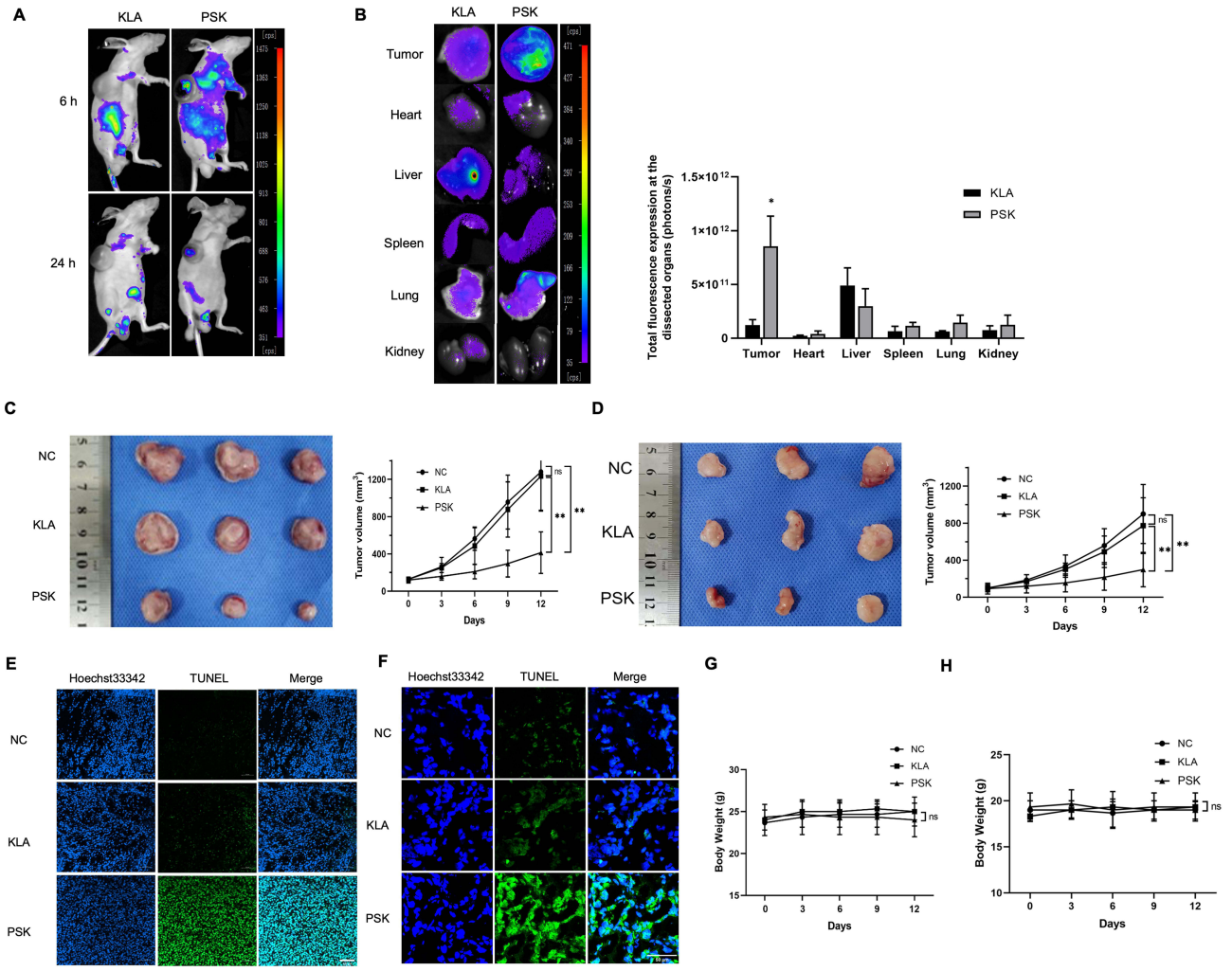

Figure 5 PSK selectively accumulates in tumor tissues and exerts antitumor effects in vivo. (**A**) Whole-body fluorescence imaging of 786-O tumor-bearing nude mice at 6 h and 24 h after intravenous injection of Cy5-labeled KLA or PSK. (**B**) Fluorescence imaging and quantitative analysis of major organs (heart, liver, spleen, lung, kidney) and tumors collected 24 h post-injection. (**C** and **D**) Representative tumor photographs and growth curves of HCT 116 (**C**) and 786-O (**D**) tumor-bearing nude mice treated with saline, KLA, or PSK. (**E** and **F**) TUNEL staining (green) of tumor tissues from HCT 116 (**E**) and 786-O (**F**) xenografts. Nuclei were stained with Hoechst 33342 (blue) (scale bar: 50 μm). (**G** and **H**) Body weight changes of HCT 116 (**G**) and 786-O (**H**) tumor-bearing nude mice during the treatment period. (NC, negative control; ns, not significant; *p < 0.05; **p < 0.01).

Additionally, immunohistochemical analysis indicated a reduction in PD-L1 levels in tumor tissues following PSK treatment (Figure S2A). To further validate the induction of ICD by PSK within tumor tissues, we performed immunofluorescence staining on tumor tissue sections to examine the key ICD marker CRT. As shown in Figure S2B, compared with the control group, PSK treatment resulted in a marked increase. This result confirms the robust induction of ICD in tumor tissues following PSK treatment. We also measured serum levels of interferon-γ (IFN-γ), a cytokine involved in the regulation of tumor cell proliferation, metastasis inhibition, anti-angiogenesis, and immune activation. IFN-γ expression was significantly upregulated in PSK-treated mice, while no notable difference was observed between the KLA and control groups (Figure S2C), suggesting that PSK may enhance antitumor immunity. To evaluate the biocompatibility of PSK, throughout the treatment period, no significant changes in body weight were observed across any of the groups (Figure 5G and H), indicating minimal systemic toxicity. Histopathological examination via HE staining of major organs (heart, liver, spleen, lung, and kidney) showed no evident damage in any treatment group (Figure S3A). In contrast, substantial tumor cell destruction was confirmed in PSK-treated mice. Furthermore, serum biochemical analysis of liver and kidney function markers-AST, ALT, ALB, UREA, and CRE-revealed no significant

https://doi.org/10.2147/IJN.S544253

differences among the groups (Figure S3B). Together, these findings demonstrate that PSK exhibits high biosafety in vivo and causes no detectable harm to normal tissues.

Discussion

In this study, we successfully designed and validated an enzyme-responsive peptide, PSK, capable of in situ self-assembly. Experimental results demonstrated that PSK efficiently targets PD-L1 and is internalized by tumor cells. Triggered by legumain, it undergoes in situ self-assembly, enabling targeted delivery of the pro-apoptotic KLA peptide and activation of the mitochondrial apoptosis pathway. Concurrently, PSK induces ICD, as evidenced by the release of DAMPs such as CRT and Hsp70, while also mediating the internalization and degradation of PD-L1. These mechanisms collectively contributed to significant inhibition of tumor growth both in vitro and in vivo. Furthermore, PSK did not induce any apparent signs of toxicity in the nude mouse model, as evidenced by the absence of significant body weight loss or tissue damage.

Recent studies have highlighted the crucial role of mitochondrial dysfunction in tumor initiation and progression, establishing mitochondrial targeting as a promising therapeutic strategy.[15] As the primary site of energy production, mitochondria are central to metabolic reprogramming in cancer cells, and their dysregulation is a key driver of oncogenesis.[45,46] Importantly, alterations in mitochondrial energy metabolism also impact the activation, proliferation, and differentiation of immune cells, influencing the activity and function of tumor-infiltrating immune cells and thereby fostering an immunosuppressive TME.[13,47] Mounting evidence indicates that mitochondrial damage leads to ROS overproduction, triggering severe oxidative stress and initiating apoptosis.[48] In the context of ICD, elevated mitochondrial ROS can further enhance the immunogenicity of dying cells.[49] For instance, ROS facilitate the translocation of CRT from the endoplasmic reticulum to the cell surface, where it serves as an "eat me" signal to promote phagocytosis by dendritic cells (DCs)—a key mechanism underlying ICD.[50] The apoptosis and ICD induced by PSK in our study are consistent with these mechanisms, providing a plausible explanation for its antitumor immune effects.

Specifically, KLA released upon legumain-mediated cleavage of PSK induces mitochondrial membrane permeabilization, activating the intrinsic apoptotic pathway. It is noteworthy that ROS burst resulting from mitochondrial damage may further trigger the integrated stress response (ISR). Our data showed that PSK treatment significantly upregulated surface exposure of CRT, providing a potent "eat me" signal for DCs.[51] This indicates that PSK-induced apoptosis is not a "silent" process but rather a form of ICD driven by mitochondrial stress.

Although the role of KLA in inducing mitochondrial apoptosis is well-established,[52,53] its clinical translation has been hampered by poor targeting efficiency and inadequate delivery.[17] Conventional nanocarriers (eg, polymeric nanoparticles), despite leveraging the EPR effect, still face limitations such as poor tumor penetration and inefficient lysosomal escape.[54] In a recent study, Wang et al developed a pyrrole-KLA monomer that was oxidatively polymerized with Cu^{2}+ to form PPy-KLA-Cu nanoparticles. This system combines photothermal therapy and enzyme-like catalytic activity, enhancing antitumor efficacy through multiple mechanisms including ROS elevation and glutathione (GSH) depletion.[37] However, the long-term toxicity and metabolic fate of such synthetic polymers and metal ions require further evaluation. Sun et al employed photo-initiated polymerization-induced self-assembly (photo-PISA) to construct core–shell nanoparticles incorporating the KLA peptide, significantly improving its stability and cellular uptake efficiency. This platform is applicable for the delivery of various functional peptides.[40] Nonetheless, the potential long-term toxicity and metabolic pathways of these synthetic polymers remain unclear. In contrast to traditional biomaterials, bioinspired nanomaterials based in situ self-assembling peptides exhibit superior biocompatibility, biodegradability, and bioactivity, emerging as promising tools for cancer immunotherapy.[55] Compared to previous studies, our approach offers several advantages: first, the all-peptide-based design may offer higher biocompatibility and avoid potential toxicity associated with synthetic materials or metal ions; second, PSK not only directly induces apoptosis but also synergistically activates antitumor immunity through ICD induction and PD-L1 degradation. However, several limitations of this study need to be addressed in future work: first, the immune synergy mediated by PSK should be further validated in immunocompetent tumor-bearing mouse models; second, the heterogeneous expression of legumain represents a potential challenge; furthermore, the long-term toxicological profile, immunogenicity, and potential impact of PSK on the autoimmune system require comprehensive evaluation.

Conclusion

This study aimed to address critical challenges in cancer immunotherapy, including suboptimal response rates, frequent acquisition of resistance, and the immunosuppressive TME, by achieving synergistic integration of ICD induction and PD-1/PD-L1 blockade. Our results demonstrate that PSK not only effectively triggers ICD and activates innate immunity, but also promotes the internalization and degradation of PD-L1, thereby alleviating immune suppression. Consequently, PSK establishes a cooperative antitumor mechanism that synergizes apoptotic cell death, innate immune activation, and restoration of adaptive immunity. Moreover, the proposed in situ self-assembly strategy offers a solution to overcome key limitations of peptide drugs, such as poor targeting efficiency and systemic toxicity, providing a novel conceptual framework for coordinated delivery of multimodal therapeutics. Nevertheless, this study has certain limitations. The pharmacokinetic profile and potential immunotoxicity of PSK warrant further investigation in large animal models. Additionally, variable expression levels of legumain across different cancer types and individual patients may influence treatment efficacy. Future work will focus on evaluating the safety and therapeutic potency of PSK in advanced animal models. In summary, this study presents a promising strategy to overcome resistance to immunotherapy and paves the way for novel approaches in precision cancer therapy.

Data Sharing Statement

All data generated or analyzed during this study are included in this published article and its supplementary information files. Other raw and relevant data from the study are available for research purposes from the corresponding authors upon reasonable request.

Ethical Statement

The animal experiment was approved by the Ethics Committee of Affiliated Central Hospital of Dalian University of Technology (document number: 2024-101-06), and the laboratory animal welfare adheres to Guidelines for Welfare and Ethical Review of Laboratory Animals (GB/T 35892-2018).

Author Contributions

All authors made a significant contribution to the work reported, whether that is in the conception, study design, execution, acquisition of data, analysis and interpretation, or in all these areas; took part in drafting, revising or critically reviewing the article; gave final approval of the version to be published; have agreed on the journal to which the article has been submitted; and agree to be accountable for all aspects of the work.

Funding

This work is supported by the Dalian Life and Health Field Guidance Project (Grant No. 2023YGZD02) and the Dalian Youth Science and Technology Star Talent Innovation Support Program (Grant No. 2024RQ097). The funders had no role in the design of the study; in the collection, analyses, or interpretation of data; in the writing of the manuscript; or in the decision to publish the results.

Disclosure

The authors declare no conflict of interest.

References

1. Vanneman M, Dranoff G. Combining immunotherapy and targeted therapies in cancer treatment, Nature reviews. *Cancer*. 2012;12(4):237–251.
2. Aldea M, Andre F, Marabelle A, Dogan S, Barlesi F, Soria JC. Overcoming resistance to tumor-targeted and immune-targeted therapies. *Cancer Discov*. 2021;11(4):874–899. doi:10.1158/2159-8290.CD-20-1638
3. Ye F, Dewanjee S, Li Y, et al. Advancements in clinical aspects of targeted therapy and immunotherapy in breast cancer. *Mol Cancer*. 2023;22(1):105. doi:10.1186/s12943-023-01805-y
4. Kroemer G, Chan TA, Eggermont AMM, Galluzzi L. Immunosurveillance in clinical cancer management. *Ca a Cancer J Clinicians*. 2024;74(2):187–202. doi:10.3322/caac.21818
5. Johnson DB, Nebhan CA, Moslehi JJ, Balko JM. Immune-checkpoint inhibitors: long-term implications of toxicity. *Nat Rev Clin Oncol*. 2022;19(4):254–267. doi:10.1038/s41571-022-00600-w
6. He X, Xu C. Immune checkpoint signaling and cancer immunotherapy. *Cell Res*. 2020;30(8):660–669. doi:10.1038/s41422-020-0343-4

7. Galluzzi L, Guilbaud E, Schmidt D, Kroemer G, Marincola FM. Targeting immunogenic cell stress and death for cancer therapy. *Nat Rev Drug Discov*. 2024;23(6):445–460. doi:10.1038/s41573-024-00920-9
8. Yamazaki T, Pitt JM, Vétizou M, et al. The oncolytic peptide LTX-315 overcomes resistance of cancers to immunotherapy with CTLA4 checkpoint blockade. *Cell Death Differ*. 2016;23(6):1004–1015. doi:10.1038/cdd.2016.35
9. Mukherjee S, Bhatti GK, Chhabra R, Reddy PH, Bhatti JS. Targeting mitochondria as a potential therapeutic strategy against chemoresistance in cancer. *Biomed Pharmacother*. 2023;160:114398. doi:10.1016/j.biopha.2023.114398
10. Wan J, Zhang X, Li Z, et al. Oxidative stress amplifiers as immunogenic cell death nanoinducers disrupting mitochondrial redox homeostasis for cancer immunotherapy. *Adv Healthc Mater*. 2023;12(9):e2202710. doi:10.1002/adhm.202202710
11. Zheng P, Ding B, Jiang Z, et al. Ultrasound-augmented mitochondrial calcium ion overload by calcium nanomodulator to induce immunogenic cell death. *Nano Lett*. 2021;21(5):2088–2093. doi:10.1021/acs.nanolett.0c04778
12. Oresta B, Pozzi C, Braga D, et al. Mitochondrial metabolic reprogramming controls the induction of immunogenic cell death and efficacy of chemotherapy in bladder cancer. *Sci Transl Med*. 2021;13(575). doi:10.1126/scitranslmed.aba6110
13. Zhang Y, Yan H, Wei Y, Wei X. Decoding mitochondria's role in immunity and cancer therapy. *Biochim Biophys Acta Rev Cancer*. 2024;1879 (4):189107. doi:10.1016/j.bbcan.2024.189107
14. Boese AC, Kang S. Mitochondrial metabolism-mediated redox regulation in cancer progression. *Redox Biol*. 2021;42:101870. doi:10.1016/j.redox.2021.101870
15. Zhou Q, Cao T, Li F, et al. Mitochondria: a new intervention target for tumor invasion and metastasis. *Mol Med*. 2024;30(1):129. doi:10.1186/s10020-024-00899-4
16. Jiang L, Li L, He X, et al. Overcoming drug-resistant lung cancer by paclitaxel loaded dual-functional liposomes with mitochondria targeting and pH-response. *Biomaterials*. 2015;52:126–139. doi:10.1016/j.biomaterials.2015.02.004
17. Hao W, Hu C, Huang Y, Chen Y. Coadministration of kla peptide with HPRP-A1 to enhance anticancer activity. *PLoS One*. 2019;14(11):e0223738. doi:10.1371/journal.pone.0223738
18. Hu C, Chen X, Huang Y, Chen Y. Synergistic effect of the pro-apoptosis peptide kla-TAT and the cationic anticancer peptide HPRP-A1. *Apoptosis*. 2018;23(2):132–142. doi:10.1007/s10495-018-1443-1
19. Lee J, Oh ET, Lee HJ, et al. Tuning of peptide cytotoxicity with cell penetrating motif activatable by matrix metalloproteinase-2. *ACS Omega*. 2022;7(34):29684–29691. doi:10.1021/acsomega.2c02127
20. Jung HK, Kim S, Park RW, Park JY, Kim IS, Lee B. Bladder tumor-targeted delivery of pro-apoptotic peptide for cancer therapy. *J Control Release*. 2016;235:259–267. doi:10.1016/j.jconrel.2016.06.008
21. Huang Y, Li X, Sha H, et al. Tumor-penetrating peptide fused to a pro-apoptotic peptide facilitates effective gastric cancer therapy. *Oncol Rep*. 2017;37(4):2063–2070. doi:10.3892/or.2017.5440
22. Fu B, Long W, Zhang Y, et al. Enhanced antitumor effects of the BRBP1 compound peptide BRBP1-TAT-KLA on human brain metastatic breast cancer. *Sci Rep*. 2015;5:8029. doi:10.1038/srep08029
23. Sun W, Li L, Li LJ, Yang QQ, Zhang ZR, Huang Y. Two birds, one stone: dual targeting of the cancer cell surface and subcellular mitochondria by the galectin-3-binding peptide G3-C12. *Acta Pharmacol Sin*. 2017;38(6):806–822. doi:10.1038/aps.2016.137
24. Li S, Zhang W, Xue H, Xing R, Yan X. Tumor microenvironment-oriented adaptive nanodrugs based on peptide self-assembly. *Chem Sci*. 2020;11 (33):8644–8656. doi:10.1039/D0SC02937H
25. Kim J, Lee S, Kim Y, et al. In situ self-assembly for cancer therapy and imaging. *Nature Rev Mater*. 2023;2023:1.
26. Yan ZL, Liu YF, Zhao LC, et al. In situ stimulus-responsive self-assembled nanomaterials for drug delivery and disease treatment. *Mater Horizons*. 2023;10(9):3197–3217. doi:10.1039/d3mh00592e
27. Cong Y, Ji L, Gao YJ, et al. Microenvironment-induced in situ self-assembly of polymer-peptide conjugates that attack solid tumors deeply. *Angew Chem Int Ed Engl*. 2019;58(14):4632–4637. doi:10.1002/anie.201900135
28. Wang MD, Lv GT, An HW, Zhang NY, Wang H. In situ self-assembly of bispecific peptide for cancer immunotherapy. *Angew Chem Int Ed*. 2022;61(10):1.
29. Wang MD, Hou DY, Lv GT, et al. Targeted in situ self-assembly augments peptide drug conjugate cell-entry efficiency. *Biomaterials*. 2021;278:121139. doi:10.1016/j.biomaterials.2021.121139
30. Liu X, Li M, Liu J, et al. In situ self-sorting peptide assemblies in living cells for simultaneous organelle targeting. *J Am Chem Soc*. 2022;144 (21):9312–9323. doi:10.1021/jacs.2c01025
31. Moon Y, Shim MK, Choi J, et al. Anti-PD-L1 peptide-conjugated prodrug nanoparticles for targeted cancer immunotherapy combining PD-L1 blockade with immunogenic cell death. *Theranostics*. 2022;12(5):1999–2014. doi:10.7150/thno.69119
32. Zheng S, Cai Y, Hong Y, et al. Legumain/pH dual-responsive lytic peptide–paclitaxel conjugate for synergistic cancer therapy. *Drug Delivery*. 2022;29(1):1764–1775. doi:10.1080/10717544.2022.2081380
33. Zheng R, Yang J, Mamuti M, et al. Controllable self-assembly of peptide-cyanine conjugates in vivo as fine-tunable theranostics. *Angew Chem Int Ed*. 2021;60(14):7809–7819. doi:10.1002/anie.202015126
34. Jia Z, Wang D, Wu R, et al. Hybrid anticancer peptide synergistically improving cancer cell uptake and inducing apoptosis mediated by membrane fusion. *Biomacromolecules*. 2025;26(4):2708–2719. doi:10.1021/acs.biomac.5c00154
35. Chen X, Lee SK, Song M, et al. RHAMM(B)-mediated bifunctional nanotherapy targeting Bcl-xL and mitochondria for pancreatic neuroendocrine tumor treatment. *Mol Ther Oncolytics*. 2021;23:277–287. doi:10.1016/j.omto.2021.10.002
36. Song C, Tang C, Xu W, et al. Hypoxia-targeting multifunctional nanoparticles for sensitized chemotherapy and phototherapy in head and neck squamous cell carcinoma. *Int J Nanomed*. 2020;15:347–361. doi:10.2147/IJN.S233294
37. Wang C, Tian X, Li X. Synthesis of a catalytic nanomaterial from polypyrrole and a pro-apoptotic peptide to target mitochondria for multimodal cancer therapy. *Org Biomol Chem*. 2024;22(24):4958–4967. doi:10.1039/d4ob00600c
38. Song C, Ran J, Wei Z, et al. Organic near-infrared-ii nanophotosensitizer for safe cancer phototheranostics and improving immune microenvironment against metastatic tumor. *ACS Appl Mater Interfaces*. 2021;13(3):3547–3558. doi:10.1021/acsami.0c18841
39. Antika G, Cinar Z, Seçen E, et al. Strigolactone analogs: two new potential bioactiphores for glioblastoma. *ACS Chem Neurosci*. 2022;13 (5):572–580. doi:10.1021/acschemneuro.1c00702

40. Sun H, Cao W, Zang N, et al. Proapoptotic peptide brush polymer nanoparticles via photoinitiated polymerization-induced self-assembly. *Angew Chem Int Ed Engl*. 2020;59(43):19136–19142. doi:10.1002/anie.202006385
41. Zhang D, Ma B, Liu D, et al. Discovery of a peptide proteolysis-targeting chimera (PROTAC) drug of p300 for prostate cancer therapy. *EBioMedicine*. 2024;105:105212. doi:10.1016/j.ebiom.2024.105212
42. Chen MY, Xiao ZK, Lei XP, et al. Preparation, characterization and in vitro-in vivo evaluation of bortezomib supermolecular aggregation nanovehicles. *J Nanobiotechnol*. 2020;18(1):57. doi:10.1186/s12951-020-00612-7
43. Li Z, Lai X, Fu S, et al. Immunogenic cell death activates the tumor immune microenvironment to boost the immunotherapy efficiency. *Adv Sci*. 2022;9(22):e2201734. doi:10.1002/advs.202201734
44. Li Q, Chen C, Kong J, Li L, Li J, Huang Y. Stimuli-responsive nano vehicle enhances cancer immunotherapy by coordinating mitochondria-targeted immunogenic cell death and PD-L1 blockade. *Acta Pharm Sin B*. 2022;12(5):2533–2549. doi:10.1016/j.apsb.2021.11.005
45. Missiroli S, Perrone M, Genovese I, Pinton P, Giorgi C. Cancer metabolism and mitochondria: finding novel mechanisms to fight tumours. *EBioMedicine*. 2020;59:102943. doi:10.1016/j.ebiom.2020.102943
46. Zong WX, Rabinowitz JD, White E. Mitochondria and cancer. *Mol Cell*. 2016;61(5):667–676. doi:10.1016/j.molcel.2016.02.011
47. Mills EL, Kelly B, O'Neill LAJ. Mitochondria are the powerhouses of immunity. *Nat Immunol*. 2017;18(5):488–498. doi:10.1038/ni.3704
48. Xu Z, Xu J, Sun S, et al. Mecheliolide elicits ROS-mediated ERS driven immunogenic cell death in hepatocellular carcinoma. *Redox Biol*. 2022;54:102351. doi:10.1016/j.redox.2022.102351
49. Yang J, Ren B, Yin X, et al. Expanded ROS generation and hypoxia reversal: excipient-free self-assembled nanotheranostics for enhanced cancer photodynamic immunotherapy. *Adv Mater*. 2024;36(30):e2402720. doi:10.1002/adma.202402720
50. Hu X, Zhang M, Quan C, Ren S, Chen W, Wang J. ROS-responsive and triple-synergistic mitochondria-targeted polymer micelles for efficient induction of ICD in tumor therapeutics. *Bioact Mater*. 2024;36:490–507. doi:10.1016/j.bioactmat.2024.06.038
51. Jiang J, Yan Y, Yang C, Cai H. Immunogenic cell death and metabolic reprogramming in cancer: mechanisms, synergies, and innovative therapeutic strategies. *Biomedicines*. 2025;13(4):1.
52. Ellerby HM, Arap W, Ellerby LM, et al. Anti-cancer activity of targeted pro-apoptotic peptides. *Nat Med*. 1999;5(9):1032–1038. doi:10.1038/12469
53. Guo Z, Li D, Peng H, et al. Specific hepatic stellate cell-penetrating peptide targeted delivery of a KLA peptide reduces collagen accumulation by inducing apoptosis. *J Drug Target*. 2017;25(8):715–723. doi:10.1080/1061186X.2017.1322598
54. Fan D, Cao Y, Cao M, Wang Y, Cao Y, Gong T. Nanomedicine in cancer therapy. *Signal Transduct Target Ther*. 2023;8(1):293. doi:10.1038/s41392-023-01536-y
55. Wen Z, Song ZZ, Cai MZ, et al. Biomimetic nanomaterials based on peptide in situ self-assembly for immunotherapy applications. *Wiley Interdiscip Rev Nanomed Nanobiotechnol*. 2025;17(1):e70005. doi:10.1002/wnan.70005